



Cite this: *J. Mater. Chem. A*, 2015, 3, 12328

## Enhanced electrochemical performance of hierarchical $\text{CoFe}_2\text{O}_4/\text{MnO}_2/\text{C}$ nanotubes as anode materials for lithium-ion batteries†

Junjie Zhou,<sup>ab</sup> Ting Yang,<sup>a</sup> Minglei Mao,<sup>a</sup> Weiji Ren<sup>a</sup> and Qihong Li<sup>\*ab</sup>

Hierarchical  $\text{CoFe}_2\text{O}_4/\text{MnO}_2/\text{C}$  nanotubes were prepared by electrospinning and a subsequent hydrothermal method. Their electrochemical properties were investigated for use as anode materials for lithium-ion batteries. The  $\text{CoFe}_2\text{O}_4/\text{MnO}_2/\text{C}$  composite displayed a stable cycling performance with a reversible capacity of  $713.6 \text{ mA h g}^{-1}$  after 250 discharge–charge cycles at a current density of  $100 \text{ mA g}^{-1}$ , much higher than that of  $\text{CoFe}_2\text{O}_4/\text{C}$  nanofibers, which displayed a capacity of  $200 \text{ mA h g}^{-1}$  after 90 cycles. The improved electrochemical performance could be ascribed to the stable hierarchical structure of the nanocomposite, the existence of carbon, the high active surface area, and the high theoretical capacity of  $\text{MnO}_2$ . Given their enhanced electrochemical performance, the  $\text{CoFe}_2\text{O}_4/\text{MnO}_2/\text{C}$  heterostructure composite can be considered as a promising anode for lithium-ion batteries.

Received 30th March 2015  
Accepted 5th May 2015

DOI: 10.1039/c5ta02305j

[www.rsc.org/MaterialsA](http://www.rsc.org/MaterialsA)

### 1. Introduction

As one of the most important energy-storage devices, lithium-ion batteries (LIBs) have great potential to meet the energy demands of a series of electronic devices, from portable devices to hybrid electric vehicles because of their high energy density, high voltage, light weight and so on.<sup>1–3</sup> Since the practical applications of LIBs highly rely on electrode materials, designing and achieving safe and low-cost electrode materials have turned into a great challenge to both academia and industries.<sup>4–6</sup> Compared with conventional carbon-based materials, transition metal oxides as negative electrodes offer more choices to realize high reversible capacities.<sup>7–9</sup> Recently, cobalt ferrite ( $\text{CoFe}_2\text{O}_4$ ) has attracted great attention due to its high gravimetric specific capacity ( $916 \text{ mA h g}^{-1}$ ), safety, low cost, and environmental friendliness.<sup>10–14</sup> However, like other transition metal oxides,  $\text{CoFe}_2\text{O}_4$  suffers from the problems of poor electrical conductivity and electrode pulverization induced by huge volume changes during the charge–discharge processes, thus leading to poor cycling stability and poor rate capability, which have greatly hampered its practical application.<sup>15</sup> Various strategies have been developed to address these problems,<sup>2,11,16–18</sup> such as combining  $\text{CoFe}_2\text{O}_4$  with graphene to improve electronic conductivity and structural stability,<sup>14,19</sup>

combining  $\text{CoFe}_2\text{O}_4$  with metal oxides to form hierarchical structures to enhance its capacity and strengthen the structural stability<sup>20,21</sup> and so on.

Hierarchical structures have been considered as promising electrode structures for advanced LIBs because they can not only integrate the merits of individual components, but also take advantage of the nanometer sized secondary building blocks.<sup>4,6,9,20–22</sup> For instance, a high capacity anode for LIBs was fabricated by coating carbon nanotubes (CNTs) with  $\text{MnO}_2$  nanosheets, thereby combining the advantages of the good electrical conductivity and large surface area of CNTs, and the short path length of  $\text{MnO}_2$  nanosheets.<sup>23,24</sup>

Herein, in order to solve the problems of  $\text{CoFe}_2\text{O}_4$  including poor electrical conductivity and poor structural stability, we can add high conductivity carbon to  $\text{CoFe}_2\text{O}_4$ . Moreover, heterostructures constructed with other metal oxides serve as protective layers to maintain the structural integrity of  $\text{CoFe}_2\text{O}_4$  during the bulk redox reaction to achieve the best performance. Manganese dioxide ( $\text{MnO}_2$ ) with high theoretical capacity ( $1230 \text{ mA h g}^{-1}$ ), relatively low electrochemical motivation force, and natural abundance<sup>23–26</sup> has been recognized as one of the intensively investigated metal oxides. It was reported that  $\text{MnO}_2$  nanoparticles grew onto a conductive polymer or a carbon layer, and the results demonstrated that it could provide a high active surface area and enhance the capacity and stability of the composite.<sup>27</sup> In this work, we grew  $\text{MnO}_2$  nanosheets on  $\text{CoFe}_2\text{O}_4/\text{C}$  nanofibers to form a heterostructure of the  $\text{CoFe}_2\text{O}_4/\text{MnO}_2/\text{C}$  composite to improve the electrochemical properties.

A facile electrospinning technique combined with a hydrothermal reaction is proposed to synthesize  $\text{CoFe}_2\text{O}_4/\text{MnO}_2/\text{C}$  nanostructures. The structures incorporated electrochemical features of individual components such as the structural

<sup>a</sup>Key laboratory for Micro-/Nano-Optoelectronic Devices of Ministry of Education, School of Physics and Electronics, Hunan University, Changsha 410082, China. E-mail: [liqihong@xmu.edu.cn](mailto:liqihong@xmu.edu.cn); Tel: +86-592-2187198

<sup>b</sup>Pen-Tung Sah Institute of Micro-Nano Science and Technology of Xiamen University, Xiamen, 361005, China

† Electronic supplementary information (ESI) available. See DOI: 10.1039/c5ta02305j

stability of a one-dimensional (1D) reticular structure with high theoretical capacity of  $\text{MnO}_2$ . Thus, on one hand,  $\text{MnO}_2$  nanosheets as shells of the composite effectively separate the as-obtained  $\text{CoFe}_2\text{O}_4$  from the electrolyte, avoiding the possible dissolution of Fe/Co species and other side-effects during the charge–discharge process. On the other hand,  $\text{CoFe}_2\text{O}_4$  acts as the core of the composite to effectively restrain the aggregation of the newly formed  $\text{Mn}^0$  and accommodate the volume change induced by the reduction of  $\text{MnO}_2$ .<sup>5,27</sup> As a result, the prepared material evaluated as an anode material for LIBs exhibited a high initial capacity of  $1560 \text{ mA h g}^{-1}$  and a stable reversible capacity of  $713.6 \text{ mA h g}^{-1}$  after 250 cycles at a current density of  $100 \text{ mA g}^{-1}$ .  $\text{CoFe}_2\text{O}_4/\text{MnO}_2/\text{C}$  showed enhanced specific capacity, long cycling life and good rate capability. The disclosure of the correlation between the electrochemical properties and the structure/component of nanocomposites would greatly benefit the rational design of high-performance nanocomposites for lithium ion batteries.

## 2. Experimental section

### 2.1 Preparation of $\text{CoFe}_2\text{O}_4/\text{C}$ nanofibers

Firstly, 1 mmol  $\text{Co}(\text{NO}_3)_2 \cdot 6\text{H}_2\text{O}$  and 2 mmol  $\text{Fe}(\text{NO}_3)_3 \cdot 9\text{H}_2\text{O}$  were dissolved in a mixture of 2.2 g ethanol and 2.2 g *N,N*-dimethyl-formamide and stirred for 1 h at room temperature. Then, 0.37 g polyvinyl pyrrolidone was dissolved in the resulting solution under magnetic stirring for 3 h at room temperature. And then the precursor solutions were pumped through a 10 mL syringe with a stainless steel nozzle (inner diameter is 0.5 mm). The precursor solutions were electrospun by applying a voltage of 20 kV using a high-voltage DC power supply at a distance of 20 cm between the nozzle tip and the collector. Then, the as-obtained nanofibers were dried at  $70^\circ\text{C}$  for 24 h in a vacuum oven, followed by calcination at  $450^\circ\text{C}$  for 2 h at a heating rate of  $1^\circ\text{C min}^{-1}$  under argon.

### 2.2 Fabrication of the $\text{CoFe}_2\text{O}_4/\text{MnO}_2/\text{C}$ composite

The prepared 0.2 g  $\text{CoFe}_2\text{O}_4/\text{C}$  nanofibers and 0.1 g  $\text{KMnO}_4$  (2 : 1 w/w) were dissolved in 40 mL deionized water and stirred for 30 min at room temperature. The solution was transferred into a Teflon-lined autoclave and the reaction temperature was maintained at  $120^\circ\text{C}$  for 8 h. After cooling to room temperature, the resulting black precipitates were washed with distilled water and ethanol several times, and then dried in a vacuum oven at  $80^\circ\text{C}$  overnight.

### 2.3 Characterization of the $\text{CoFe}_2\text{O}_4/\text{C}$ and $\text{CoFe}_2\text{O}_4/\text{MnO}_2/\text{C}$ materials

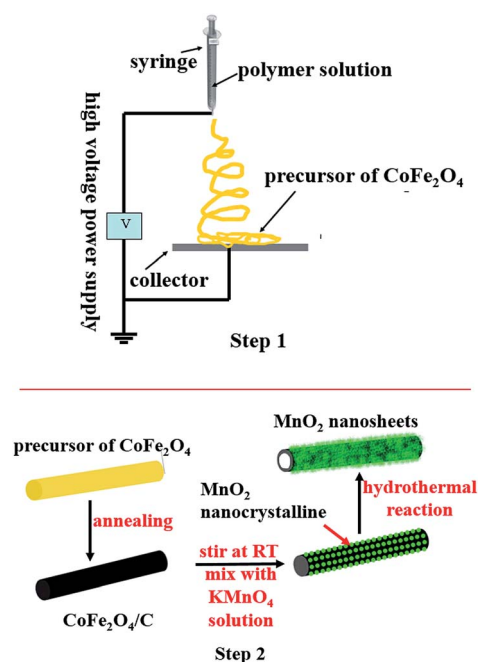
The crystal structures of the samples were characterized by X-ray diffraction (XRD,  $\text{Cu K}\alpha$  irradiation) with a SIEMENS D5000 X-ray diffractometer. The morphology and microstructure of the synthesized sample were characterized by scanning electron microscopy (SEM, Hitachi S4800 equipped with an EDS) and a transmission electron microscope (TEM; JEOL-2010) with an accelerating voltage of 200 kV.

### 2.4 Electrochemical measurements of $\text{CoFe}_2\text{O}_4/\text{C}$ and $\text{CoFe}_2\text{O}_4/\text{MnO}_2/\text{C}$ materials

The electrochemical properties of the  $\text{CoFe}_2\text{O}_4/\text{MnO}_2/\text{C}$  material were evaluated by assembling coin-type cells in an argon-filled glove box. For preparing the working electrodes, the active material, carbon black and carboxyl methyl cellulose (CMC) were mixed in a weight ratio of 80 : 10 : 10, and in distilled water and absolute alcohol mixture, stirred at a constant speed for 12 h to form a homogeneous slurry, which was spread uniformly on a copper foil. The coated copper foil was cut into round pieces with a diameter of 1 cm, and dried at  $80^\circ\text{C}$  in a vacuum overnight. The mass loading of the active material was about  $0.8 \text{ mg cm}^{-2}$ . A Celgard 2400 microporous polypropylene membrane was used as a separator. The electrolyte contained a solution of 1 M  $\text{LiPF}_6$  in ethylene carbonate/dimethyl carbonate/diethyl carbonate (1 : 1 : 1, in wt%). These cells were assembled in a glove box (Super 1220/750, Switzerland) filled with highly pure argon gas ( $\text{O}_2$  and  $\text{H}_2\text{O}$  levels less than 1 ppm). The cells were aged for 12 h before measurement to ensure percolation of the electrolyte to the electrodes. Cyclic voltammetry and galvanostatic cycling were performed using an Arbin BT2000 system in the voltage range of 0.01–3.0 V (vs.  $\text{Li}^+/\text{Li}$ ). Nyquist plots were recorded using a CHI660e electrochemical work station at selected voltages ranging from 0.01–3.0 V (vs.  $\text{Li}^+/\text{Li}$ ) and frequencies ranging from 0.01 Hz to 1 MHz at room temperature.

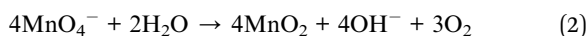
## 3. Results and discussion

The fabrication process of the precursor of  $\text{CoFe}_2\text{O}_4/\text{C}$  nanofibers is presented in step 1 of Scheme 1. The growth of the  $\text{CoFe}_2\text{O}_4/\text{MnO}_2/\text{C}$  nanocomposite is illustrated in step 2 of



Scheme 1 Illustration of the synthesis process of  $\text{CoFe}_2\text{O}_4/\text{MnO}_2/\text{C}$  nanotubes.

Scheme 1. Briefly, the resulting products of step 1 were subjected to calcination at 450 °C for 2 h at a heating rate of 1 °C min<sup>-1</sup> under argon, and carbon was obtained in CoFe<sub>2</sub>O<sub>4</sub> nanofibers. And then CoFe<sub>2</sub>O<sub>4</sub>/C nanofibers were dispersed well in a KMnO<sub>4</sub> solution at room temperature. Nanocrystalline MnO<sub>2</sub> would be formed on the surface of the CoFe<sub>2</sub>O<sub>4</sub>/C nanofibers due to the slow redox process according to eqn (1).<sup>28</sup> When the solution was further treated by a hydrothermal process, the preformed nanocrystalline MnO<sub>2</sub> acted as nucleation sites for MnO<sub>2</sub> nanosheets to continuously grow due to the redox reaction between C and KMnO<sub>4</sub> according to eqn (1) and the decomposition of KMnO<sub>4</sub> in water according to eqn (2). Therefore MnO<sub>2</sub> nanosheets could be uniformly coated on the surfaces of CoFe<sub>2</sub>O<sub>4</sub>/C and the CoFe<sub>2</sub>O<sub>4</sub>/MnO<sub>2</sub>/C hierarchical nanocomposite was obtained.



The SEM image of the CoFe<sub>2</sub>O<sub>4</sub>/C nanofibers is shown in Fig. 1a. The CoFe<sub>2</sub>O<sub>4</sub>/C fibers exhibited a smooth surface morphology with diameters ranging from 50 to 90 nm. Moreover, from Fig. S1a (in the ESI†) we can see that the CoFe<sub>2</sub>O<sub>4</sub>/C nanofibers exhibit a solid structure. Fig. 1b–d show SEM images of the CoFe<sub>2</sub>O<sub>4</sub>/MnO<sub>2</sub>/C composite. Obviously, after coating MnO<sub>2</sub> nanosheets, the composite not only became thick with diameters larger than 100 nm, but also became rough and brushy. It is seen from Fig. 1c and d that the MnO<sub>2</sub> nanosheets were uniformly coated on CoFe<sub>2</sub>O<sub>4</sub>/C nanotubes to form a core-shell structure with plenty of room which could alleviate the volume change during the lithium-ion intercalation-deintercalation process. As shown in Fig. 1d, the CoFe<sub>2</sub>O<sub>4</sub>/MnO<sub>2</sub>/C composite was hollow, and the diameter of the holes was about 40 nm, which could not only effectively shorten the lithium-ion and electron transport path along the 1D geometry hollow

nanotubes, but also alleviate the volume change of CoFe<sub>2</sub>O<sub>4</sub> during the charge–discharge process. Moreover, Fig. S1b (in the ESI†) further shows that the CoFe<sub>2</sub>O<sub>4</sub>/MnO<sub>2</sub>/C composite exhibits a hollow structure. By comparing Fig. S1a with Fig. S1b,† we can see that the solid structure of CoFe<sub>2</sub>O<sub>4</sub>/C nanofibers transformed into a hollow structure of the CoFe<sub>2</sub>O<sub>4</sub>/MnO<sub>2</sub>/C composite *via* the hydrothermal reaction, which could be induced by the consumption of partial carbon of CoFe<sub>2</sub>O<sub>4</sub>/C nanofibers due to the redox reaction between C and KMnO<sub>4</sub> according to eqn (1) during the hydrothermal reaction. Moreover, by comparing Fig. 1a with Fig. S1b,† we can see that CoFe<sub>2</sub>O<sub>4</sub>/MnO<sub>2</sub>/C nanotubes decreased in length after the hydrothermal reaction. The reason that CoFe<sub>2</sub>O<sub>4</sub>/C nanofibers appeared fractured could be related to the reaction of KMnO<sub>4</sub> with carbon in CoFe<sub>2</sub>O<sub>4</sub>/C fibers during the MnO<sub>2</sub> coating process. As shown in Fig. 1b and c, after coating MnO<sub>2</sub> nanosheets, CoFe<sub>2</sub>O<sub>4</sub>/MnO<sub>2</sub>/C nanotubes were connected to each other to form a reticular structure, thus leading to good structural stability of CoFe<sub>2</sub>O<sub>4</sub>/MnO<sub>2</sub>/C electrodes during the charge–discharge process.

The detailed structures of the products were also examined by TEM. Fig. 2a displays the TEM image of CoFe<sub>2</sub>O<sub>4</sub>/C fibers. Fig. 2b shows typical TEM images of the CoFe<sub>2</sub>O<sub>4</sub>/MnO<sub>2</sub>/C composite in which ultrathin MnO<sub>2</sub> nanosheets are uniformly distributed on the surface of the CoFe<sub>2</sub>O<sub>4</sub>/C. A close examination of the exposed profile revealed that the thickness of the outer MnO<sub>2</sub> layer was about 30 nm. A high-resolution TEM (HRTEM) image of the CoFe<sub>2</sub>O<sub>4</sub>/MnO<sub>2</sub>/C hybrid structure shown in Fig. 2d reveals two interplanar spacings of 0.25 nm and 0.48 nm, corresponding to the (311) and (111) planes of CoFe<sub>2</sub>O<sub>4</sub>,<sup>14</sup> respectively. An interplanar spacing of 0.46 nm corresponds to the (111) plane of MnO<sub>2</sub>,<sup>26</sup> which is in agreement with the XRD results (Fig. 3).

Fig. 3 shows the XRD pattern of the as-prepared CoFe<sub>2</sub>O<sub>4</sub>/MnO<sub>2</sub>/C nanotubes. Three diffraction peaks appear at 30.28°, 35.54° and 62.58°, which can be respectively attributed to (220),

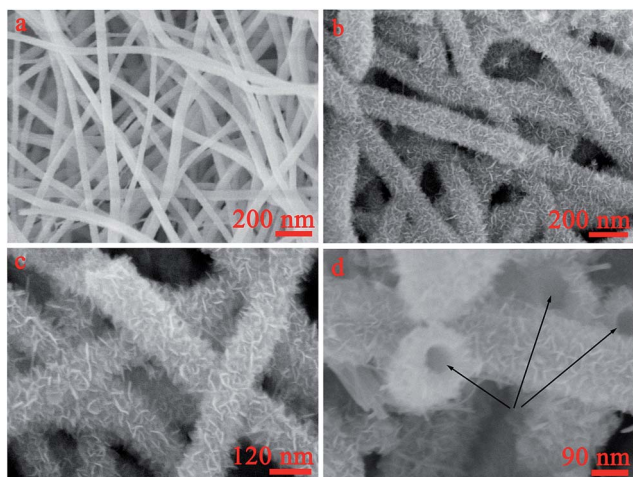


Fig. 1 SEM images of (a) CoFe<sub>2</sub>O<sub>4</sub>/C nanofibers; (b–d) CoFe<sub>2</sub>O<sub>4</sub>/MnO<sub>2</sub>/C composite at different magnifications.

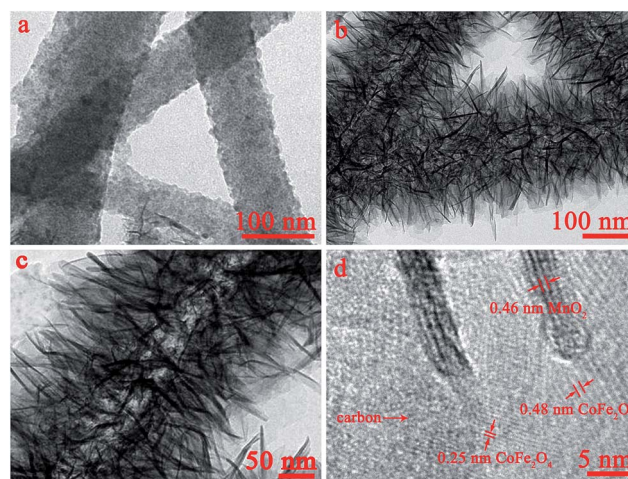


Fig. 2 (a) TEM image of CoFe<sub>2</sub>O<sub>4</sub>/C nanofibers; (b and c) TEM images of the CoFe<sub>2</sub>O<sub>4</sub>/MnO<sub>2</sub>/C composite; (d) HRTEM image of the CoFe<sub>2</sub>O<sub>4</sub>/MnO<sub>2</sub>/C composite.



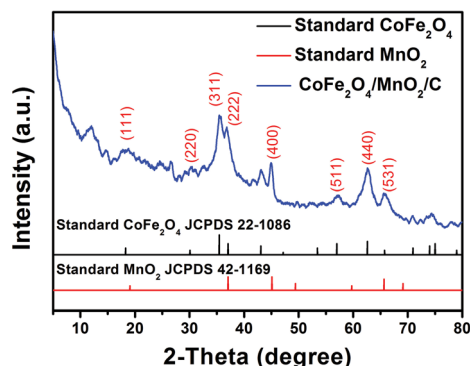


Fig. 3 XRD pattern of the  $\text{CoFe}_2\text{O}_4/\text{MnO}_2/\text{C}$  composite (blue), standard  $\text{CoFe}_2\text{O}_4$  (black) and standard  $\text{MnO}_2$  (red).

(311) and (440) reflections of spinel  $\text{CoFe}_2\text{O}_4$  (JCPDS 22-1086). The diffraction peaks appear at  $19.22^\circ$ ,  $37.14^\circ$ ,  $45.02^\circ$  and  $67.21^\circ$  and are attributed to (111), (311), (400) and (531) reflections of  $\text{MnO}_2$  (JCPDS 42-1169). A broad band at about  $25.6^\circ$  can be indexed to the carbon phase.<sup>13</sup> The XRD pattern revealed that the resulting sample consisted of  $\text{CoFe}_2\text{O}_4$ ,  $\text{MnO}_2$  and amorphous carbon. We also carried out an energy dispersive spectroscopic (EDS) analysis of the composite. The EDS spectrum is shown in Fig. S2 in the ESI.† The results indicated the existence of manganese, iron, cobalt, and carbon in the composite. Thermogravimetric analysis (TGA) was conducted to estimate the weight of carbon in the composite, which was about 31 wt% as indicated in Fig. S3 in the ESI.†

Fig. 4 shows the cyclic voltammograms of the  $\text{CoFe}_2\text{O}_4/\text{MnO}_2/\text{C}$  electrode between 0.01 and 3.00 V (vs.  $\text{Li}/\text{Li}^+$ ) at a scan rate of  $0.1 \text{ mV s}^{-1}$ . In the first cycle, a cathodic peak at about 0.2 V could be ascribed to the reduction of  $\text{MnO}_2$  to metallic manganese as well as the formation of a solid electrolyte interface (SEI), and the other cathodic peak at around 0.59 V could be attributed to the reduction of  $\text{Fe}^{3+}$  and  $\text{Co}^{2+}$  to their metallic states and the formation of  $\text{Li}_2\text{O}$  and a SEI. In the anodic process, an anodic peak at about 1.2 V corresponds to the oxidation of metallic manganese.<sup>26</sup> And a broad peak at around 1.8 V could be ascribed to the multi-oxidation steps of metallic Co and Fe to  $\text{Co}^{2+}$  and  $\text{Fe}^{3+}$ , respectively.<sup>29</sup> Compared

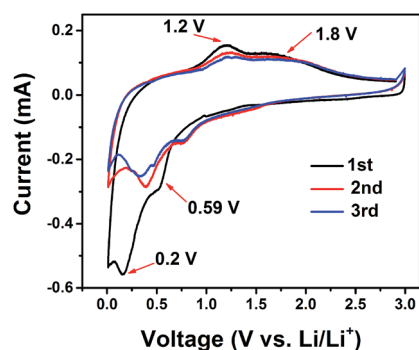
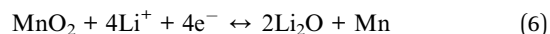
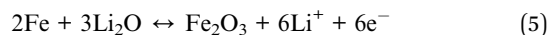


Fig. 4 Cyclic voltammetry (CV) of the  $\text{CoFe}_2\text{O}_4/\text{MnO}_2/\text{C}$  composite at a scan rate of  $0.1 \text{ mV s}^{-1}$ .

with the first cycle, due to the structure reconstruction induced by the formation of  $\text{Li}_2\text{O}$  and metals, the cathodic peaks of the subsequent cycles shifted to higher potentials, which further confirmed multi-step electrochemical reactions.<sup>30</sup> An obvious decrease of the areas enclosed by CV curves from the first to the second cycle indicated an irreversible capacity loss in the initial lithiation/delithiation process, usually attributed to the occurrence of irreversible reactions associated with formation of an SEI layer. The results, to a certain extent, sustained the electrochemical reactions for the anode material as follows:



The charge–discharge curves for the prepared  $\text{CoFe}_2\text{O}_4/\text{C}$  and  $\text{CoFe}_2\text{O}_4/\text{MnO}_2/\text{C}$  anodes with a current density of  $100 \text{ mA g}^{-1}$  are shown in Fig. 5a and b. The initial charge capacities were  $970.9 \text{ mA h g}^{-1}$  for  $\text{CoFe}_2\text{O}_4/\text{C}$  and  $1583.8 \text{ mA h g}^{-1}$  for the  $\text{CoFe}_2\text{O}_4/\text{MnO}_2/\text{C}$  electrode, respectively. The increased capacity for the  $\text{CoFe}_2\text{O}_4/\text{MnO}_2/\text{C}$  nanocomposite was not only from mechanical amalgamation, but an inter-enhancement effect of these two compositions.<sup>21</sup> The large capacity loss in the first cycle for these electrodes was caused by the formation of a SEI on the electrode surface due to the electrolyte decomposition.<sup>31–33</sup> Fig. 5b clearly shows a voltage plateau at 0.59 V in the first discharge, reflecting the conversion reaction of  $\text{Fe}^{3+}$  and  $\text{Co}^{2+}$  to their metallic states,<sup>34</sup> which is in agreement with the results in Fig. 4 of cyclic voltammetry (CV) for the  $\text{CoFe}_2\text{O}_4/\text{MnO}_2/\text{C}$  composite.

Stable cyclic performance is important for an electrode material for its practical application in LIBs. The cycling stabilities of the  $\text{CoFe}_2\text{O}_4/\text{MnO}_2/\text{C}$  composite and  $\text{CoFe}_2\text{O}_4/\text{C}$  nanofibers were investigated at a current density of  $100 \text{ mA g}^{-1}$  between 0.01 and 3.0 V (Fig. 6a). The discharge capacity of the  $\text{CoFe}_2\text{O}_4/\text{MnO}_2/\text{C}$  electrode remained at  $713.6 \text{ mA h g}^{-1}$  after 250 cycles, and the coulombic efficiency was around 99%, indicating a stable cyclability. In contrast, the  $\text{CoFe}_2\text{O}_4/\text{C}$  nanofibers only delivered a much lower capacity of  $200 \text{ mA h g}^{-1}$  after 90 discharge–charge cycles. Moreover, the capacity of

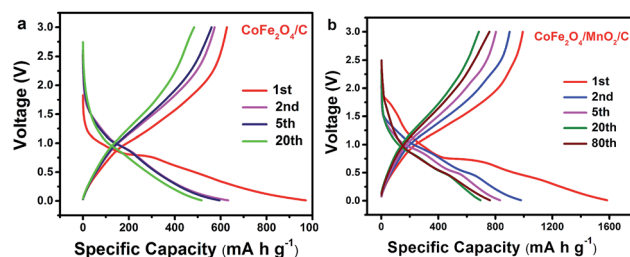


Fig. 5 Charge–discharge curves of (a)  $\text{CoFe}_2\text{O}_4/\text{C}$  and (b)  $\text{CoFe}_2\text{O}_4/\text{MnO}_2/\text{C}$  at a current density of  $100 \text{ mA g}^{-1}$ .

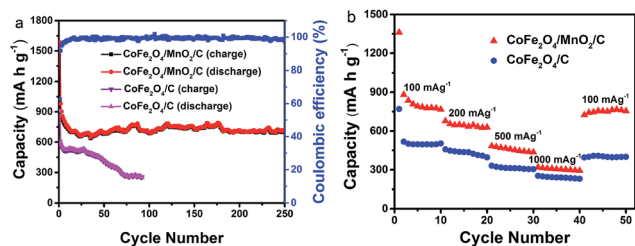


Fig. 6 (a) Cycling performance of  $\text{CoFe}_2\text{O}_4/\text{C}$  and  $\text{CoFe}_2\text{O}_4/\text{MnO}_2/\text{C}$  heterostructures at a current density of  $100 \text{ mA g}^{-1}$ . (b) Rate performance of the  $\text{CoFe}_2\text{O}_4/\text{MnO}_2/\text{C}$  composite and  $\text{CoFe}_2\text{O}_4/\text{C}$  anodes.

$\text{CoFe}_2\text{O}_4/\text{MnO}_2/\text{C}$  increased slightly with cycling, which was also observed in many metal oxide anode materials.<sup>35–37</sup> The reasons for the increase of capacity during cycling could be ascribed to the reversible growth of a polymer gel-like film caused by kinetically activated electrolyte degradation and the activation of the active materials.<sup>38–42</sup> The high electrochemical performance of the core-shell nanomaterials was mainly related to the following factors: (1) the hollow structure could not only facilitate lithium-ion access, but also accommodate large volumetric expansion to slow down the rate of electrode pulverization; (2)  $\text{MnO}_2$  nanosheets and high conductivity carbon buffer layers served as protective layers to maintain the structural integrity during the bulk redox reaction; after coating  $\text{MnO}_2$  nanosheets,  $\text{CoFe}_2\text{O}_4/\text{MnO}_2/\text{C}$  nanotubes were connected to each other to form a reticular structure, thus leading to good structural stability of  $\text{CoFe}_2\text{O}_4/\text{MnO}_2/\text{C}$  electrodes; and (3)  $\text{MnO}_2$  nanosheets as the shells of the composite effectively separated the as-obtained  $\text{CoFe}_2\text{O}_4$  from the electrolyte, avoiding the possible dissolution of Fe/Co species and other side-effects during the charge-discharge process. Meanwhile,  $\text{CoFe}_2\text{O}_4$  acted as a core to restrain the aggregation of newly formed  $\text{Mn}^0$  and accommodate the volume change induced by the reduction of  $\text{MnO}_2$ .<sup>5,27</sup>  $\text{CoFe}_2\text{O}_4/\text{MnO}_2/\text{C}$  nanotubes showed enhanced cycling properties, better than a series of reported  $\text{CoFe}_2\text{O}_4$  or  $\text{MnO}_2$  composites. As shown in Table S1,<sup>†</sup> long stable cycling and high capacity were obtained as compared with some reported  $\text{CoFe}_2\text{O}_4$  and  $\text{MnO}_2$  materials or their composites.

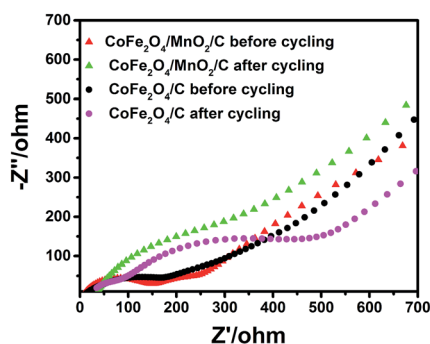


Fig. 7 Impedance spectra of  $\text{CoFe}_2\text{O}_4/\text{C}$  and  $\text{CoFe}_2\text{O}_4/\text{MnO}_2/\text{C}$  electrodes.

To examine the rate performance of the  $\text{CoFe}_2\text{O}_4/\text{MnO}_2/\text{C}$  electrode, the discharge capacities of  $\text{CoFe}_2\text{O}_4/\text{MnO}_2/\text{C}$  were measured at different discharge current densities. Fig. 6b shows the rate performance of  $\text{CoFe}_2\text{O}_4/\text{MnO}_2/\text{C}$  and  $\text{CoFe}_2\text{O}_4/\text{C}$  electrodes. For  $\text{CoFe}_2\text{O}_4/\text{MnO}_2/\text{C}$ , the average discharge capacities of 799.8, 648.8, 470.4, and  $310.6 \text{ mA h g}^{-1}$  were observed at the current densities of 100, 200, 500, and  $1000 \text{ mA g}^{-1}$ , respectively. For comparison,  $\text{CoFe}_2\text{O}_4/\text{C}$  delivered capacities of 497.9, 423.5, 310.8, and  $237.8 \text{ mA h g}^{-1}$ , when the current densities were 100, 200, 500 and  $1000 \text{ mA g}^{-1}$ , respectively. When the current density was returned to  $100 \text{ mA g}^{-1}$ , the discharge capacity of the  $\text{CoFe}_2\text{O}_4/\text{MnO}_2/\text{C}$  electrode could recover to  $762.9 \text{ mA h g}^{-1}$ . However, the  $\text{CoFe}_2\text{O}_4/\text{C}$  electrode only displayed a capacity of  $397 \text{ mA h g}^{-1}$ . The enhanced rate performance of the  $\text{CoFe}_2\text{O}_4/\text{MnO}_2/\text{C}$  electrode was related to the following properties: firstly, the hollow structure allowed the electrolyte to easily diffuse into the interior of the composite and reduced the resistance of the transported lithium-ions; secondly, the high surface area increased the contact between the electrode and electrolyte and provided a large number of potential active sites for the  $\text{Li}^+$  transfer reaction; thirdly, the existence of the carbon layer improved the conductivity of the electrode. The high capacity achieved at a high cycling rate implies that this type of electrode can be a promising candidate for high power applications.

Electrochemical impedance spectroscopy (EIS) provides detailed information on charge transfer, surface film, bulk resistance and capacitance of the electrodes.<sup>43</sup> EIS was carried out on  $\text{CoFe}_2\text{O}_4/\text{MnO}_2/\text{C}$  at selected frequencies ranging from 0.01 Hz to 1 MHz at room temperature. All impedance spectra exhibited a single semicircle in a high frequency region, which was related to the charge transfer resistance ( $R_{\text{ct}}$ ), and a sloping line in a low frequency region, representing the Warburg impedance ( $Z_w$ ) induced by lithium-ion diffusion in the electrodes.<sup>44</sup> Fig. 7 shows the electrochemical impedance of  $\text{CoFe}_2\text{O}_4/\text{MnO}_2/\text{C}$  and  $\text{CoFe}_2\text{O}_4/\text{C}$  before cycling and after 200 cycles. Before cycling, the  $R_{\text{ct}}$  value of  $\text{CoFe}_2\text{O}_4/\text{MnO}_2/\text{C}$  and  $\text{CoFe}_2\text{O}_4/\text{C}$  displayed little difference. After 200 cycles, it was obvious that the  $R_{\text{ct}}$  value of  $\text{CoFe}_2\text{O}_4/\text{MnO}_2/\text{C}$  was lower than that of  $\text{CoFe}_2\text{O}_4/\text{C}$ . As expected, the hierarchical  $\text{CoFe}_2\text{O}_4/\text{MnO}_2/\text{C}$  nanotube electrode exhibited a rapid charge transfer reaction during lithium insertion and extraction. The results indicated that the  $\text{CoFe}_2\text{O}_4/\text{MnO}_2/\text{C}$  nanocomposite electrode exhibited enhanced electrochemical performance.

## 4. Conclusions

In summary, electrospinning and a subsequent hydrothermal method were developed to synthesize core-shell  $\text{CoFe}_2\text{O}_4/\text{MnO}_2/\text{C}$  nanotubes. The hollow core-shell structure provided a sufficient electrode-electrolyte interface and alleviated the large strain caused by the conversion reaction of the electrode, and was also beneficial to the lithium-ion and electron transportation. As a result, the  $\text{CoFe}_2\text{O}_4/\text{MnO}_2/\text{C}$  heterostructure anode showed a high initial capacity of  $1580.6 \text{ mA h g}^{-1}$  and a reversible capacity of  $713.6 \text{ mA h g}^{-1}$  after 250 cycles at  $100 \text{ mA g}^{-1}$ , a long cycling life and a good rate performance. The highly

improved electrochemical performance was ascribed to the stable hierarchical structure of the nanocomposite, the existence of the carbon layer, the high active surface area and the high theoretical capacity of  $\text{MnO}_2$ .  $\text{MnO}_2$  sheets were proposed to serve as protective layers to maintain the structural integrity of  $\text{CoFe}_2\text{O}_4$  during the bulk redox reaction. The study shows that the  $\text{CoFe}_2\text{O}_4/\text{MnO}_2/\text{C}$  heterostructure is a promising anode material for LIBs.

## Acknowledgements

This work was partly supported by the Specialized Research Fund for the Doctoral Program of Higher Education of China (20120161110016), and the National Natural Science Foundation of China (Grant no. 61376073).

## Notes and references

- 1 J. G. Kim, S. H. Lee, Y. Kim and W. B. Kim, *ACS Appl. Mater. Interfaces*, 2013, **5**, 11321–11328.
- 2 N. Wang, H. Xu, L. Chen, X. Gu, J. Yang and Y. Qian, *J. Power Sources*, 2014, **247**, 163–169.
- 3 Z. Xing, Z. Ju, J. Yang, H. Xu and Y. Qian, *Nano Res.*, 2012, **5**, 477–485.
- 4 R. Zhang, Y. He, A. Li and L. Xu, *Nanoscale*, 2014, **6**, 14221–14226.
- 5 X. Gu, L. Chen, Z. Ju, H. Xu, J. Yang and Y. Qian, *Adv. Funct. Mater.*, 2013, **23**, 4049–4056.
- 6 Q. Q. Xiong, J. P. Tu, X. H. Xia, X. Y. Zhao, C. D. Gu and X. L. Wang, *Nanoscale*, 2013, **5**, 7906–7912.
- 7 G. Wang, R. Chen, Y. Zhou, H. Wang and J. Bai, *J. Nanopart. Res.*, 2014, **16**, 2300.
- 8 J. Liu, J. Jiang, M. Bosman and H. J. Fan, *J. Mater. Chem.*, 2012, **22**, 2419–2426.
- 9 A. K. Rai, J. Gim, T. V. Thi, D. Ahn, S. J. Cho and J. Kim, *J. Phys. Chem. C*, 2014, **118**, 11234–11243.
- 10 Y. N. NuLi and Q. Z. Qin, *J. Power Sources*, 2005, **142**, 292–297.
- 11 Y. Q. Chu, Z. W. Fu and Q. Z. Qin, *Electrochim. Acta*, 2004, **49**, 4915–4921.
- 12 Y. Wang, D. Su, A. Ung, J. Ahn and G. Wang, *Nanotechnology*, 2012, **23**, 055402.
- 13 L. Wu, Q. Xiao, Z. Li, G. Lei, P. Zhang and L. Wang, *Solid State Ionics*, 2012, **215**, 24–28.
- 14 H. Xia, D. Zhu, Y. Fu and X. Wang, *Electrochim. Acta*, 2012, **83**, 166–174.
- 15 Z. H. Li, T. P. Zhao, X. Y. Zhan, D. S. Gao, Q. Z. Xiao and G. T. Lei, *Electrochim. Acta*, 2010, **55**, 4594–4598.
- 16 Z. Zhang, Y. Wang, M. Zhang, Q. Tan, X. Lv, Z. Zhong and F. Su, *J. Mater. Chem. A*, 2013, **1**, 7444–7450.
- 17 H. Xia, D. Zhu, Y. Fu and X. Wang, *Electrochim. Acta*, 2012, **83**, 166–174.
- 18 S. Li, A. Li, R. Zhang, Y. He, Y. Zhai and L. Xu, *Nano Res.*, 2014, **7**, 1116–1127.
- 19 Y. Yao, Z. Yang, D. Zhang, W. Peng, H. Sun and S. Wang, *Ind. Eng. Chem. Res.*, 2012, **51**, 6044–6051.
- 20 G. Huang, F. Zhang, X. Du, J. Wang, D. Yin and L. Wang, *Chem.–Eur. J.*, 2014, **20**, 11214–11219.
- 21 X. Li, Y. Chen, H. Yao, X. Zhou, J. Yang, H. Huang, Y.-W. Mai and L. Zhou, *RSC Adv.*, 2014, **4**, 39906–39911.
- 22 B. Wang, X. He, H. Li, Q. Liu, J. Wang, L. Yu, H. Yan, Z. Li and P. Wang, *J. Mater. Chem. A*, 2014, **2**, 12968–12973.
- 23 J. Zhao, Z. Tao, J. Liang and J. Chen, *Cryst. Growth Des.*, 2008, **8**, 2799–2805.
- 24 H. Lai, J. Li, Z. Chen and Z. Huang, *ACS Appl. Mater. Interfaces*, 2012, **4**, 2325–2328.
- 25 L. Li, A. R. O. Raji and J. M. Tour, *Adv. Mater.*, 2013, **25**, 6298–6302.
- 26 H. Xia, M. Lai and L. Lu, *J. Mater. Chem.*, 2010, **20**, 6896–6902.
- 27 J. Liu, J. Jiang, C. Cheng, H. Li, J. Zhang, H. Gong and H. J. Fan, *Adv. Mater.*, 2011, **23**, 2076–2081.
- 28 C. X. Guo, M. Wang, T. Chen, X. W. Lou and C. M. Li, *Adv. Energy Mater.*, 2011, **1**, 736–741.
- 29 X. Yao, J. Kong, X. Tang, D. Zhou, C. Zhao, R. Zhou and X. Lu, *RSC Adv.*, 2014, **4**, 27488–27492.
- 30 Y. Wang, J. Park, B. Sun, H. Ahn and G. Wang, *Chem.–Asian J.*, 2012, **7**, 1940.
- 31 B. Zhang, Y. Liu, Z. Huang, S. Oh, Y. Yu, Y. W. Mai and J. K. Kim, *J. Mater. Chem.*, 2012, **22**, 12133–12140.
- 32 X. Li, Y. Chen, L. Zhou, Y.-W. Mai and H. Huang, *J. Mater. Chem. A*, 2014, **2**, 3875–3880.
- 33 L. Wang, Y. Li, Z. Han, L. Chen, B. Qian, X. Jiang, J. Pinto and G. Yang, *J. Mater. Chem. A*, 2013, **1**, 8385–8397.
- 34 W. Xiao, J. S. Chen, Q. Lu and X. W. Lou, *J. Phys. Chem. C*, 2010, **114**, 12048–12051.
- 35 P. L. Taberna, S. Mitra, P. Poizot, P. Simon and J. M. Tarascon, *Nat. Mater.*, 2006, **5**, 567–573.
- 36 Y. Fu, X. Li, X. Sun, X. Wang, D. Liu and D. He, *J. Mater. Chem.*, 2012, **22**, 17429–17431.
- 37 Y. Xia, W. Zhang, Z. Xiao, H. Huang, H. Zeng, X. Chen, F. Chen, Y. Gan and X. Tao, *J. Mater. Chem.*, 2012, **22**, 9209–9215.
- 38 S. Grugeon, S. Laruelle, L. Dupont and J. M. Tarascon, *Solid State Sci.*, 2003, **5**, 895–904.
- 39 S. Laruelle, S. Grugeon, P. Poizot, M. Dollé, L. Dupont and J.-M. Tarascon, *J. Electrochem. Soc.*, 2002, **149**, A627–A634.
- 40 Y. Yu, C. H. Chen, J. L. Shui and S. Xie, *Angew. Chem., Int. Ed.*, 2005, **44**, 7085–7089.
- 41 L. Yu, Z. Wang, L. Zhang, H. B. Wu and X. W. Lou, *J. Mater. Chem. A*, 2013, **1**, 122–127.
- 42 Y. Lu, K. Qiu, D. Zhang, J. Lin, J. Xu, X. Liu, C. Tang, J.-K. Kim and Y. Luo, *RSC Adv.*, 2014, **4**, 46814–46822.
- 43 B. Das, M. V. Reddy, C. Krishnamoorthi, S. Tripathy, R. Mahendiran, G. V. S. Rao and B. V. R. Chowdari, *Electrochim. Acta*, 2009, **54**, 3360–3373.
- 44 S. Hu, F. Yin, E. Uchaker, W. Chen, M. Zhang, J. Zhou, Y. Qi and G. Cao, *J. Phys. Chem. C*, 2014, **118**, 24890–24897.